Nanomechanical properties of Mg-Al intermetallic compounds produced by Packed Powder Diffusion Coating (PPDC) on the surface of AZ91E

H.-W. Chang, M.-X. Zhang*, A. Atrens and H. Huang*

School of Mechanical and Mining Engineering, The University of Queensland, Brisbane, Qld 4072, Australia

Abstract

A packed powder diffusion coating (PPDC) treatment produced two intermetallic layers on the surface of the commercial magnesium alloy AZ91E. The β-phase ($Mg_{17}Al_{12}$) was immediately on top of the AZ91E, on top of which was the τ-phase ($Mg_{32}(Al,Zn)_{49}$). Nanoindentation showed that the elastic modulus and hardness of each of the intermetallic compounds was significantly greater than that of the AZ91E substrate. Staircase displacement bursts occurred during nanoindentation of the intermetallic compounds, attributed to the combination of incipient plasticity at low loads, and the development of dislocation networks due to dislocation pile ups around the indentation at higher loads. Crystallographic analysis of β phase orientations using EBSD showed that the nanomechanical properties of the intermetallic compound produced through PPDC treatment were isotropic.

Keywords: Magnesium alloy; intermetallic compound; Nanoindentation; diffusion coating; EBSD

1. Introduction

Magnesium (Mg) alloys are widely used in engineering applications due to their high strength-to-weight ratio [1]. Their major drawbacks are relatively low wear and low corrosion resistance [2], which have considerably limited their wider application. Surface modification is an effective

* Corresponding authors: School of Mechanical and Mining Engineering, The University of Queensland, St Lucia, QLD 4072, Australia; Tel.: +61 7 33468709, +61 7 33653583; Fax: +61 7 33467105, +61 7 33654799; Email: mingxing.zhang@uq.edu.au, han.huang@uq.edu.au.

approach to enhance surface durability without changing the mechanical properties [3]. Aluminizing via diffusion coating is a promising approach to improve wear and corrosion resistance [4-9]. Aluminizing forms intermetallic compounds on the surface of Mg alloys, such as the intermetallic phase β-$Mg_{17}Al_{12}$, which increase hardness and wear resistance [8]. These can also enhance corrosion resistance [10-13]. Surface durability is expected to increase with increasing volume fraction of the β phase in the aluminized layer.

However, most surface aluminizing treatments of Mg alloys are carried out at temperatures above 430 °C [6, 14-17], whereas the eutectic temperature for Mg-Al system is only 437 °C. At such high temperatures, hot cracks occur frequently in both the substrate and the alloyed layer, as a result of the local melting at eutectic areas. To overcome hot cracking, Zhang and Kelly [18] developed the packed powder diffusion coating (PPDC) technique, and introduced Zn into the Al powder so that a thick alloy layer was produced on an AZ91D alloy substrate after treatment below 430 °C. Hirmke et al. [19] refined the PPDC technique by adding more Zn, and produced thicker and more effective aluminized layers consisting of τ-$Mg_{32}(Al,Zn)_{49}$ and β-$Mg_{17}Al_{12}$ on AZ91. However, the mechanical properties of the β ($Mg_{17}Al_{12}$) and τ ($Mg_{32}(Al,Zn)_{49}$) phases have not been characterised, because the focus of the previous studies was on the optimisation of the PPDC process.

The present research to aims to characterise the mechanical properties of these intermetallic phases *in-situ* in such coatings using nanoindentation.

2. Experimental details

Specimens for the packed powder diffusion coating (PPDC) treatment were cut from a cast commercial AZ91E ingot, which had the following chemical composition: 8.31 wt.% Al, 0.52 wt.% Zn, 0.6 wt.% Mn, and remainder Mg. The grain size was approximately 500 μm. The specimen size was 15 mm x 10 mm x 10 mm. The specimens were buried in a mixture of powders (10 wt.% Zn plus 90 wt. % Al) in a steel container. The particle sizes were in the range of 15 to 75 μm. The

container was filled about two thirds with the Mg alloy specimens in the Al and Zn powder mixture, topped up with sand, on which was placed a mixture of sand and charcoal to reduce oxidation of the specimens. The PPDC treatment was carried at 413 °C for 18 hours followed by air cooling to room temperature [5, 19]. The temperature of 413 °C was selected because this temperature is typical for solid solution heat treatment for AZ91, and the maximum Al concentration could be obtained in the Mg solid solution without melting due to eutectic formation. Previous study [5] had found that the Mg-Al intermetallic coating produced by the PPDC process at 413 °C had the best corrosion resistance. After the PPDC treatment, the specimens were cross-sectioned, mounted in resin and ground and polished. The thickness of the intermetallic layers was measured on the cross sections using optical microscopy. Electron backscattered diffraction (EBSD) was performed in a JEOL 7001 scanning electron microscope to determine the orientations of individual grains within the intermetallic layers. Nanoindentation was performed on both the β and τ phases and the AZ91E substrate using a Hysitron Triboindenter®, with a three sided Berkovich indenter, with tip radius of 100 nm. The indentation load was 3000 μN. The loading /unloading rate was 100 μN per second. There was a stabilized period of 5 seconds between loading and unloading [20]. An atomic force microscope (AFM) was used to examine the surface topographies prior to, and after each indentation. The reduced elastic modulus and nanoindentation hardness (hardness in short thereinafter) were calculated from the load-displacement curves [21].

3. Results and discussion

Fig. 1(a) presents an optical micrograph of a typical intermetallic layer on the AZ91E substrate after the PPDC treatment at 413 °C for 18 hours. The 250 μm thick intermetallic coating consisted of two layers, as in previous work [5]. The top layer with a thickness of ~175 μm consisted of the τ-phase with composition $Mg_{32}(Al, Zn)_{49}$. The 75 μm thick second layer consisted of the β-phase with composition $Mg_{17}(Al, Zn)_{12}$. The EBSD analysis shown in Fig. 1(b) indicated that the β-phase layer contained equiaxed grains with an average grain size of 60 μm, and the τ-phase layer consisted of

columnar grains. Fig. 1(c) presents the distribution of grain orientation along the normal direction (ND) in an inversed pole figure (IPF), indicating that there was no obvious texture in the intermetallic layers. Fig. 1(d) presents a typical TEM micrograph of the τ and β phases and a typical τ/β interface produced by focused ion beam (FIB) etching. There were no pores within β-phase and τ-phase layers, both intermetallic layers were fully dense, and there were no pores at the interface.

Nanoindentation mapping was performed on cross-sections of the PPDC treated specimens to characterize the nanomechanical properties of the τ and β phases. The local crystallographic orientations in the nanoindentation mapping area were measured using electron backscattered diffraction (EBSD) and are presented in Fig. 2(a). The difference in the grey level in the β-phase layer indicates β grains with different crystallographic orientations. Fig. 2(a) also presents an EDS line scan showing the composition of Mg (red), Al (green) and Zn (blue) with depth into the coating. The Al and Mg contents were consistent with the compositions of the τ and β phases, and that of AZ91E. In addition there was Zn in the intermetallic layers, with a somewhat higher concentration towards the surface. This was consistent with that previously reported [19].

Nanoindentation mapping was carried out under constant conditions. An array of 18 × 21 indents was made in an area of 180 × 200 μm^2. The elastic modulus of the τ and β phases were evaluated using the elastic modulus of 1141 GPa and the Poisson's ratio of 0.07 for the diamond indenter [20] and a nominal Poisson's ratio of 0.29 for the intermetallic phases. Figs. 2(b) and (c) present the values of hardness and elastic modulus, plotted as a function of depth from the specimen surface. Fig. 2(b) shows that the hardness of the τ phase was similar to that of the β phase. The hardness of both the intermetallic compounds was approximately 4 times larger than that of the AZ91E substrate. For most materials, higher hardness is associated with greater sliding wear resistance.

Fig. 2(c) shows that the elastic modulus of the β phase was larger than that of the τ phase and both were significantly greater than that of the substrate. The higher elastic moduli of the

intermetallic phases are attributed to their stronger atomic bonds, which are considered to be a mixture of metallic and covalent bonds, because the difference in electronegativity (E) between Mg, Al and Zn is small.

The values of the modulus and hardness were lower at the interface between the intermetallic layers. This is attributed to an edge effect. Phase boundaries between τ and β or β and AZ91E are weaker than the bulk phase because plastic flow occurs more easily near a boundary as a result of lower constraint. Therefore, lower values of the hardness and modulus are typically measured near boundaries and free surfaces.

The error bars for the elastic modulus of the AZ91E substrate in Fig. 2(c) were relatively large, with the highest values close to the β phase. This is attributed to the fact that the boundary was not straight between the β phase and the AZ91E. The indents in the AZ91E closer to the boundary had some probability to have a contribution from the β phase, and these would produce a higher value of modulus. In contrast, values more representative for the substrate were measured further from the boundary, and consequently these measurements had lower scatter.

Fig. 3(a) shows typical nanoindentation load-displacement curves for the τ phase, the β phase, and the AZ91E substrate. There were numerous displacement bursts on the loading curves for the τ and β phases. Such staircase or zigzag deformation is common in the indentation of bulk single crystals of Au [22], and polycrystalline thin films of Al and Cu [23]. The displacement burst is normally considered to be associated with (i) incipient plasticity, (ii) development of dislocation networks, (iii) mechanical instability, and (iv) phase transformations. Incipient plasticity often occurs upon the earliest stages of the mechanical contact, corresponding to the transition from elastic to plastic deformation [24]. Beyond initial yield during nanoindentation, additional displacement burst events at higher loads were associated with the development of dislocation networks, including the nucleation of dislocations and their subsequent propagation into the crystals, dislocation multiplication, and the evolution of a complex defect structure [25]. Mechanical instabilities and serrated flow occur also in crystalline metals due to the interaction of dislocations

and mobile solute atoms [26]. There are no dislocations in amorphous metals or metal glasses, and plastic deformation is inherently unstable, occurring in bursts of highly localized strain, called shear banding events [27]. Phase transformations occur in many materials when they are subjected to large hydrostatic stresses, such as during nanoindentation [28]. The displacement bursts observed in the present work are attributed to the incipient plasticity and the development of dislocation networks.

Fig. 3(b) shows a magnified version of the start of the load-displacement (p-h) curves, shown by the black rectangle in Fig. 3(a). The first displacement burst occurred at around 25 nm for both intermetallic phases, and corresponded to a load of 177 μN for the β phase, and 212 μN for the τ phase. The corresponding maximum shear stress underneath the indenter tip for a displacement burst, τ_{max}, was computed to be 8.5 for the β phase, and 8.2 GPa for the τ phase. These values of τ_{max} were computed from [29]

$$\tau_{max} = 0.31\left(\frac{6PE^{*2}}{\pi^3 R^2}\right)^{1/3} \quad (1)$$

where E^* is reduced elastic modulus obtained from the p-h curves, R is the tip radius and P is the load for displacement burst. These estimates exceed the estimate of the theoretical shear strength of 3.5-4.8 GPa for the β-phase, which is estimated as $\mu_s/2\pi$ GPa, where the shear modulus of β phase, μ_s, is taken to be in the range 22 to 30 GPa based on the first-principle calculations and experimental measurement [30-32]. These estimates indicate that the maximum shear stress beneath the indenter was equal to or exceeded the theoretical shear strength, which satisfied the stress condition for inducing the incipient plasticity.

No similar comparison can be done for the τ-phase, because there are no published data for the shear modulus.

Figs. 3(c) and (d) present typical AFM images of the nanoindents on the β phase and τ phase. The triangular impressions of the indents appeared sharp, but pile ups around the indenter (white region along the indentation) were also evident for both phases. The plastic response of a material subjected to indentation is a plastic zone like an expanding cavity, which expands radially beneath

the indenter, and is confined by the adjacent elastic material [33, 34]. This expanding cavity model can be considered as a series of prismatic dislocation loops that are punched out into the material to accommodate the indenter [35, 36]. Pile-ups are generated by the rotation of the crystalline material around the indenter, and the relaxation engendered by the unloading of the indenter [37]. These pile-ups may be the cause of the displacement burst at higher loads. In contrast, Figs. 3(a) and (e) show that the load-displacement curve for AZ91E was relatively smooth, without any apparent pile-up.

Fig. 4(a) shows the EBSD mapping of the β phase layer over an area of 200 × 150 μm^2, carried out in order to examine the effect of grain orientation on the elastic modulus. The grains were numbered and their ND orientations are presented in Fig. 4(b). An array of 21 × 16 indentations were performed in this area. Fig. 4(c) presents the map of the elastic modulus, in which a bicubic interpolation was used between the measurement points. The numbered grains were divided into three groups according to their pole directions of [001], [101] and [111]. Table 1 presents the orientation of each grain with respect to the respective pole direction, and the corresponding elastic modulus, E_r. The measured elastic modulus of the β phase was in the range of 78-80 GPa. The influence of orientation on elastic modulus was not significant.

This measured result can be compared with the theoretical modulus for a grain with orientation [hkl] aligned with the loading axis, evaluated from [38]

$$\frac{1}{E_{(hkl)}} = S_{11} + (2S_{12} - 2S_{11} + S_{44})A_{(hkl)} \quad (2)$$

where S_{11}, S_{12} and S_{44} are the compliances of the material, and the anisotropy factor is given by $A_{hkl} = (h^2k^2 + k^2l^2 + l^2h^2)/(h^2 + k^2 + l^2)^2$ for a cubic crystal. For the β phase, first-principle method calculations [31] gave S_{11} = 13.836 ×10^{-3} GPa^{-1}, S_{12} = -3.46 ×10^{-3} GPa^{-1} and S_{44} = 50 ×10^{-3} GPa^{-1}. The calculated modulus for [001], [101] and [111] were 72, 57 and 53 GPa, respectively, which indicated that the [111] direction has the lowest modulus and [001] has the highest modulus.

The experimental results obtained from nanoindentation mapping (Table 1) showed the same trend that the [001] direction had the largest modulus, and the [111] direction has the lowest value. But the difference of measured modulus in those directions was insignificant compared with those from the theoretical evaluation. The cause of the small influence of orientation on the measured elastic modulus may be related to the complexity of crystal structure of the β phase, which reduces the difference in number of atomic bonds in different directions.

Fig. 5(a) presents the modulus map obtained from the nanoindentation map performed on the cross-sectional specimen shown in Fig. 2(a). Fig. 5(b) shows the variation of the modulus within each β grain with distance from the τ/β interface. As the PPDC process is a diffusion control process, the Zn and Al concentration decreased with increasing depth from the surface as shown in Fig. 2(a). However, Figs. 5(a) and (b) show that the modulus varied from 75-80 GPa, and that there was no significant change with deceasing concentration of Zn and Al solute, which indicated that the elastic modulus did not vary with the variation of solute concentration of Zn and Al.

4. Conclusions

(1) PPDC treatment produced an intermetallic compound surface coating, consisting of τ phase and β phases, which had similar values of elastic modulus and hardness, and the values were larger than those of the AZ91E substrate.

(2) Staircase displacement bursts typically occurred during nanoindentation, attributed to incipient plasticity and the development of dislocation networks.

(3) Crystallographic grain orientation using EBSD analysis indicated that the elastic modulus of the β phase layer was isotropic.

Acknowledgements

The authors would like to thank the ARC linkage project (LP110200800) for financial support.

References

[1] M.K. Kulekci, Magnesium and its alloys applications in automotive industry, International Journal of Advanced Manufacturing Technology 39 (2008) 851-865.

[2] G. Song, A. Atrens, Understanding Magnesium Corrosion—A Framework for Improved Alloy Performance, Advanced Engineering Materials 5 (2003) 837-858.

[3] L. Xianghuai, Recent advance in surface treatment and its applications in China, Surface and Coatings Technology 131 (2000) 261-266.

[4] J.E. Gray, B. Luan, Protective coatings on magnesium and its alloys — a critical review, Journal of Alloys and Compounds 336 (2002) 88-113.

[5] J. Hirmke, M.X. Zhang, D.H. StJohn, Surface alloying of AZ91E alloy by Al–Zn packed powder diffusion coating, Surface and Coatings Technology 206 (2011) 425-433.

[6] H. Yang, X. Guo, G. Wu, W. Ding, N. Birbilis, Electrodeposition of chemically and mechanically protective Al-coatings on AZ91D Mg alloy, Corrosion Science 53 (2011) 381-387.

[7] M. He, L. Liu, Y. Wu, Z. Tang, W. Hu, Improvement of the properties of AZ91D magnesium alloy by treatment with a molten AlCl3–NaCl salt to form an Mg–Al intermetallic surface layer, Journal of Coatings Technology and Research 6 (2009) 407-411.

[8] M.X. Zhang, H. Huang, K. Spencer, Y.N. Shi, Nanomechanics of Mg–Al intermetallic compounds, Surface and Coatings Technology 204 (2010) 2118-2122.

[9] H.Q. Sun, Y.N. Shi, M.X. Zhang, K. Lu, Surface alloying of an Mg alloy subjected to surface mechanical attrition treatment, Surface and Coatings Technology 202 (2008) 3947-3953.

[10] M.C. Zhao, M. Liu, G. Song, A. Atrens, Influence of the β-phase morphology on the corrosion of the Mg alloy AZ91, Corrosion Science 50 (2008) 1939-1953.

[11] G. Song, A. Atrens, M. Dargusch, Influence of microstructure on the corrosion of diecast AZ91D, Corrosion Science 41 (1998) 249-273.

[12] N. Pebere, C. Riera, F. Dabosi, Investigation of magnesium corrosion in aerated sodium sulfate solution by electrochemical impedance spectroscopy, Electrochimica Acta 35 (1990) 555-561.

[13] G.L. Song, A. Atrens, Corrosion Mechanisms of Magnesium Alloys, Advanced engineering Materials 1 (1999) 11-33.

[14] I. Shigematsu, M. Nakamura, N. Saitou, Surface treatment of AZ91D magnesium alloy by aluminum diffusion coating, Journal of Materials Science Letters 19 (2000) 473-475.

[15] M. Youping, X. Kewei, W. Weixin, H. Xipeng, L. Pengfei, The effect of solid diffusion surface alloying on properties of ZM5 magnesium alloy, Surface and Coatings Technology 190 (2005) 165-170.

[16] M. Youping, W. Weixin, L. Pengfei, X. Kewei, Effects of Treatment Parameters on Microstructure of Diffusion Alloyed Coatings on Pure Magnesium, Surface Engineering 20 (2004) 108-112.

[17] F. Liu, W. Liang, X. Li, X. Zhao, Y. Zhang, H. Wang, Improvement of corrosion resistance of pure magnesium via vacuum pack treatment, Journal of Alloys and Compounds 461 (2008) 399-403.

[18] M.-X. Zhang, P.M. Kelly, Surface alloying of AZ91D alloy by diffusion coating, Journal of Materials Research 17 (2002) 2477-2479.

[19] J. Hirmke, M.X. Zhang, D.H. St John, Influence of Chemical Composition of Mg Alloys on Surface Alloying by Diffusion Coating, Metallurgical and Materials Transactions A 43 (2012) 1621-1628.

[20] H. Huang, K. Winchester, Y. Liu, X.Z. Hu, C.A. Musca, Determination of mechanical properties of PECVD silicon nitride thin films for tunable MEMS Fabry-Perot optical filters, Journal of Micromechanics and Microengineering 15 (2005) 608-614.

[21] W.C. Oliver, G.M. Pharr, Measurement of hardness and elastic modulus by instrumented indentaiton: Advances inunderstanding and refinements to methodology, Journal of Materials Research 19 (2004) 3-20.

[22] S.G. Corcoran, R.J. Colton, Anomalous plastic deformation at surface: Nanoindentation of gold single crystals, Physical Review B 55 (1997) R16057.

[23] A. Gouldstone, H.J. Koh, K.Y. Zeng, A.E. Giannakopoulos, S. Suresh, Discrete and continuous deformation during nanoindentation of thin films, Acta Materialia 48 (2000) 2277-2295.

[24] C.A. Schuh, A.C. Lund, Application of nucleation theory to the rate dependence of incipient plasticity during nanoindentation, Journal of Materials Research 19 (2004) 2152-2158.

[25] A.M. Minor, J.J.W. Morris, E.A. Stach, Quantitative in situ nanoindentation in an electron microscope, Applied Physics Letters 79 (2001) 1625-1627.

[26] G. Bérces, N.Q. Chinh, A. Juháasz, J. Lendvai, Occurrence of plastic instabilities in dynamic microhardness testing, Journal of Materials Research 13 (1998) 1411-1413.

[27] C.A. Schuh, T.G. Nieh, A nanoindentation study of serrated flow in bulk metallic glasses, Acta Materialia 51 (2003) 87-99.

[28] J.-i. Jang, M.J. Lance, S. Wen, T.Y. Tsui, G.M. Pharr, Indentation-induced phase transformations in silicon: influences of load, rate and indenter angle on the transformation behavior, Acta Materialia 53 (2005) 1759-1770.

[29] K.L. Johnson, Contact Mechanics, Cambridge University Press, Cambridge, 1985.

[30] Z.-w. Huang, Y.-h. Zhao, H. Hou, Y.-h. Zhao, X.-f. Niu, P.-d. Han, Structural, thermodynamics and elastic properties of Mg17Al12, Al2Y and Al4Ba phases by first-principles calculations, Journal of Central South University 19 (2012) 1475-1481.

[31] Na Wang, Wei-Yang Yu, Bi-Yu Tang, L.-M. Peng, W.-J. Ding, Structural and mechanical properties of $Mg_{17}Al_{12}$ and $Mg_{24}Y_5$ from first-principles calculations, Journal of Physics D: Applied Physics 41 (2008) 195408.

[32] M. Gharghouri, Study of the Mechanical properties of Mg-8.5wt%Al by In-situ Neutron Diffraction, in The School of Graduate, 1996, McMaster University. p. 128.

[33] K.L. Johnson, The correlation of indentation experiments, Journal of the Mechanics and Physics of Solids 18 (1970) 115-126.

[34] D.M. Marsh, Plastic Flow in Glass, Proceedings of the Royal Society of London. Series A. Mathematical and Physical Sciences 279 (1964) 420-435.

[35] A. Smakula, M.W. Klein, The Plastic Deformation and Crystal Orientation of Thallium Halides, Journal of the Optical Society of America 39 (1949) 445-453.

[36] F. Seitz, Prismatic dislocations and prismatic punching in crystals, Physical Review 79 (1950) 723-724.

[37] R. Hill, E.H. Lee, S.J. Tupper, The Theory of Wedge Indentation of Ductile Materials, Proceedings of the Royal Society of London. Series A. Mathematical and Physical Sciences 188 (1947) 273-289.

[38] W.F. Hosford, The Mechanics of Crystals and Textured Polycrystals, Oxford University Press, Oxford, 1993.

List of Figure captions

Fig. 1 (a) A typical optical micrograph showing both the τ phase and β phase layers on top of the AZ91E substrate after PPDC treatment at 413 °C for 18 hours; (b) EBSD mapping on the cross-section showing the grain size; (c) grain orientation distribution along the direction normal to the surface (i.e. the ND direction); and (d) TEM observation of the β and τ phases and the β/τ interface.

Fig. 2 (a) EBSD mapping on a typical cross-section specimen, the difference in grey level in the β phase layer indicated different grain orientations, and an EDS line scan showing the variation of concentration of Mg (red), Al(green) and Zn (blue); (b) hardness, and (c) elastic modulus values plotted as a function of the depth measured from the outmost surface.

Fig. 3 (a) Load-displacement curves obtained from nanoindentation on the τ phase, the β phase and the AZ91E substrate; (b) low load part of (a); and (c), (d), (e) AFM images of the nanoindents on the τ phase, the β phase and the AZ91E substrate.

Fig. 4 (a) EBSD mapping and (b) inversed pole figure obtained from the β phase layer (the grains have been numbered for easy identification) after removal of the τ phase layer; and (c) elastic modulus map obtained from the nanoindentation mapping array shown in (a).

Fig. 5 (a) Modulus map obtained from nanoindentation testing on the cross-section specimen (β phase grains have been numbered); and (b) average modulus for each grain as a function of distance away from the τ/β interface.

Table 1. The grains with different orientation and their reduced elastic modulus, E_r

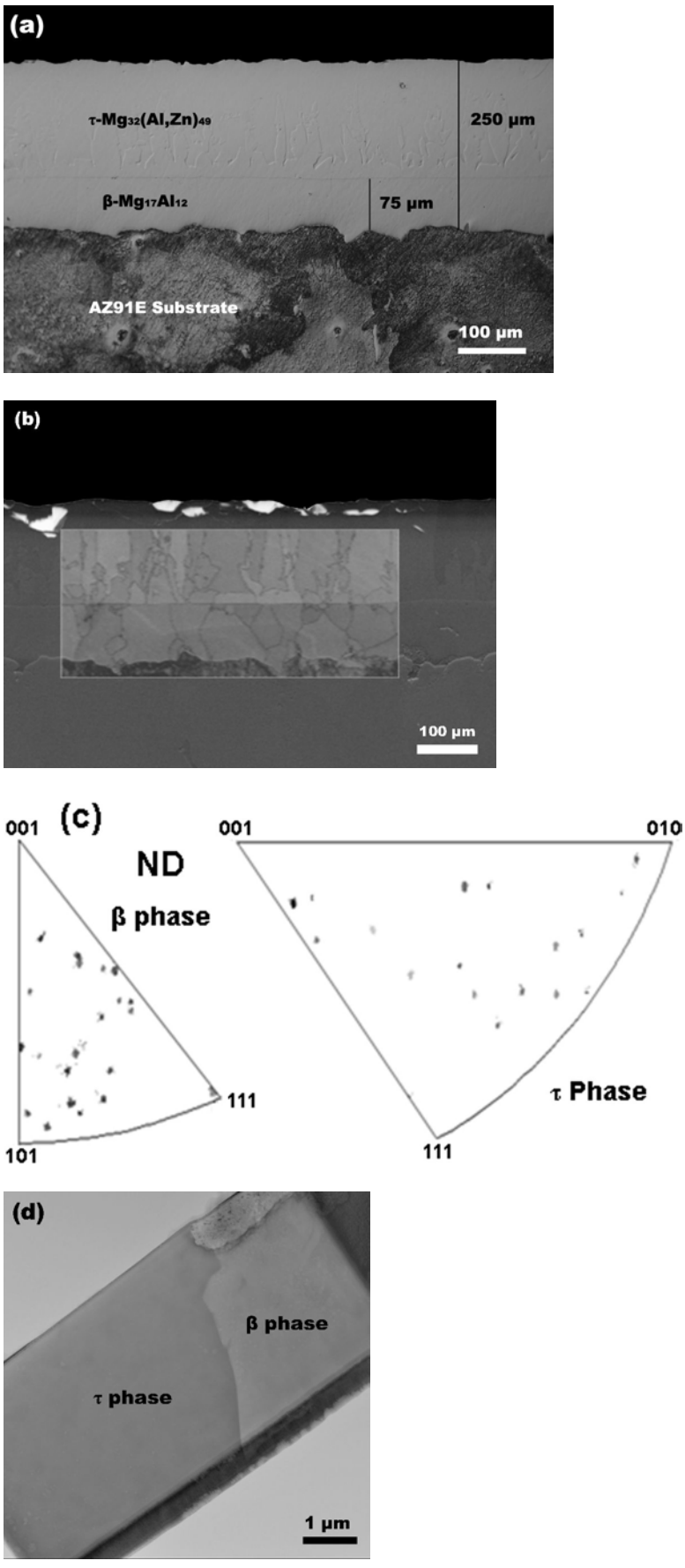
(a)
τ-Mg32(Al,Zn)49
250 μm
β-Mg17Al12
75 μm
AZ91E Substrate
100 μm
(b)
100 μm
(c)
001
ND
β phase
111
101
001
010
τ Phase
111
(d)
β phase
τ phase
1 μm

Fig. 1

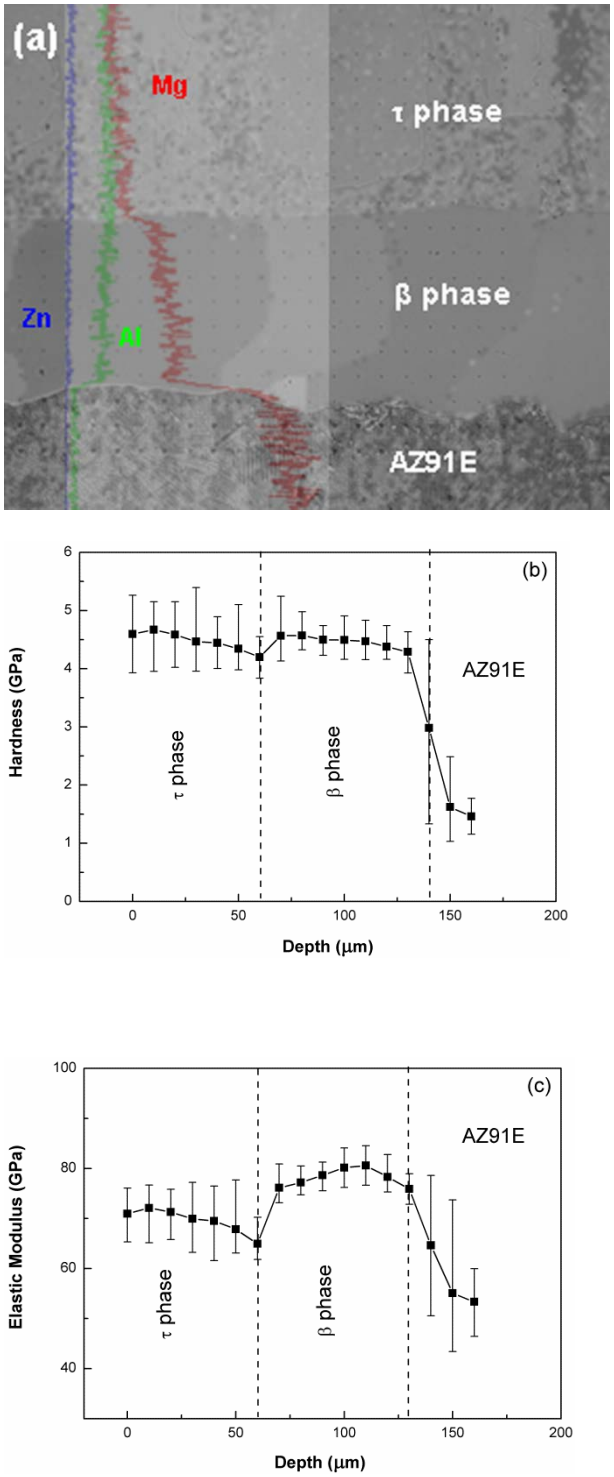
(a)
Mg
τ phase
β phase
Zn
Al
AZ91E
(b)
Hardness (GPa)
AZ91E
τ phase
β phase
Depth (μm)
(c)
Elastic Modulus (GPa)
AZ91E
τ phase
β phase
Depth (μm)

Fig. 2

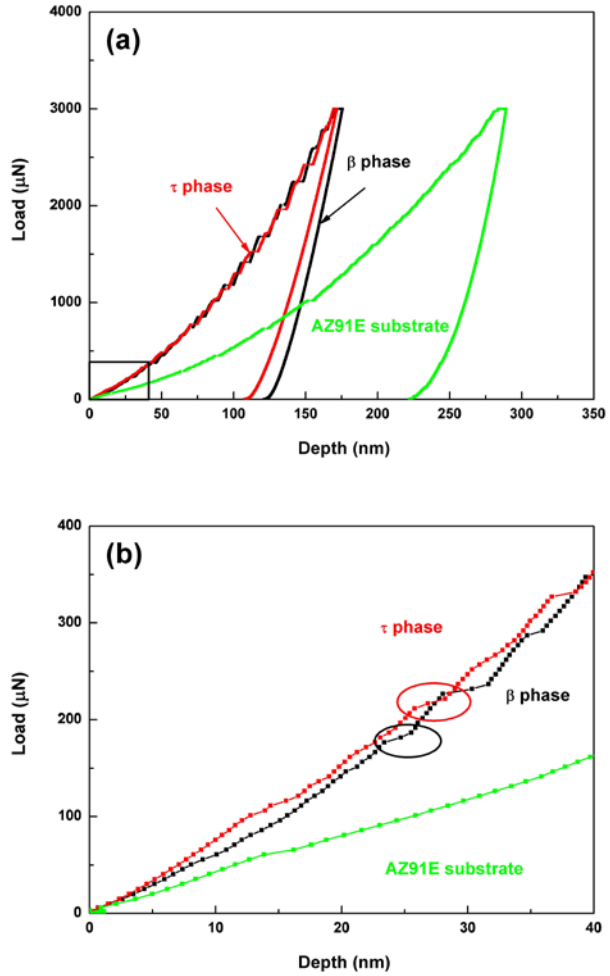
(a)
τ phase
β phase
AZ91E substrate
Load (μN)
Depth (nm)
(b)
τ phase
β phase
AZ91E substrate
Load (μN)
Depth (nm)

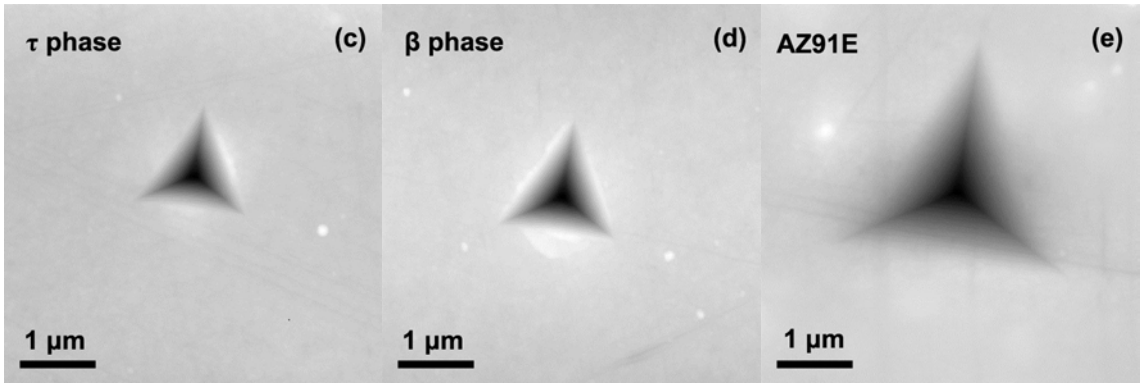
τ phase
(c)
1 μm
β phase
(d)
1 μm
AZ91E
(e)
1 μm

Fig. 3

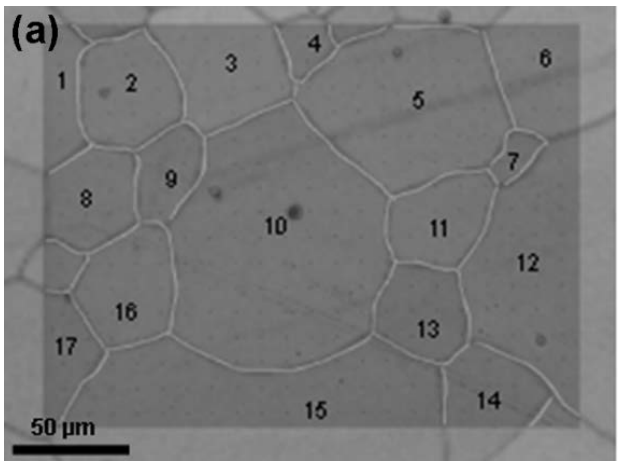
(a)
1
2
3
4
5
6
7
8
9
10
11
12
13
14
15
16
17
50 µm

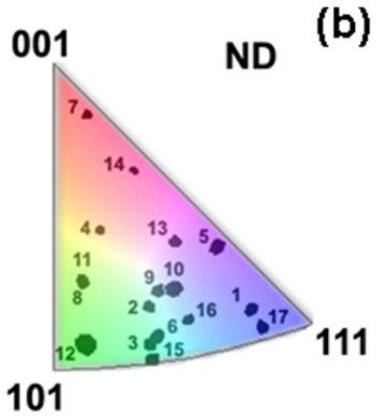
(b)
001
ND
111
101

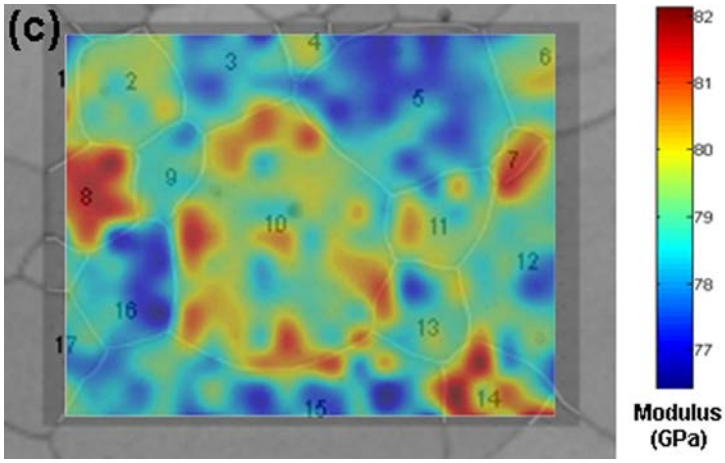
(c)
82
81
80
79
78
77
Modulus
(GPa)

Fig. 4

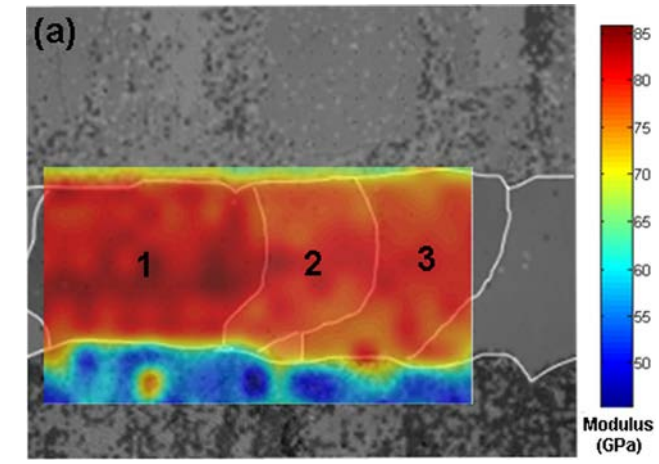
(a)
1
2
3
85
80
75
70
65
60
55
50
Modulus
(GPa)

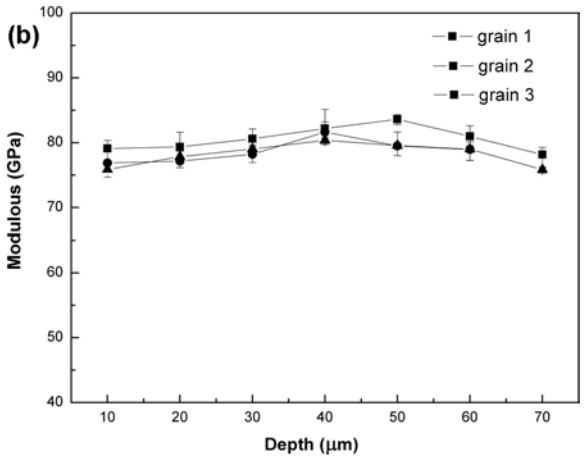
(b)
grain 1
grain 2
grain 3
Modulous (GPa)
Depth (μm)
100
90
80
70
60
50
40
10
20
30
40
50
60
70

Fig. 5

Table 1 The grains with different orientation and their reduced elastic modulus

β-$Mg_{17}Al_{12}$					
	Grain No.	Orientation(φ_1, Φ, φ_2)	misorientation	E_r	Average value of E_r of grains near pole
Near [111]	17	94.5, 50.1, 38.3	7° from (111)	78.6 ± 0.6	78.8
	1	210.9, 46.3, 51.2	9° from (111)	79.4 ± 1.3	
	5	192.1, 35.8, 41.7	19° from (111)	77.8 ± 0.8	
	16	183.4, 42.5, 62.0	19° from (111)	78.1 ± 0.8	
	10	93.0, 37.3, 62.5	22° from (111)	79.7 ± 1.0	
	13	60.7, 31.3, 55.5	25° from (111)	78.9 ± 0.7	
Near [101]	12	105.4, 41.2, 6.2	9° from (101)	78.9 ± 0.6	79.1
	15	288.8, 45.9, 71.7	13° from (101)	78.2 ± 0.9	
	2	247.8, 38.1, 68.4	14° from (101)	79.2 ± 0.6	
	8	68.4, 32.1, 8.4	14° from (101)	81.0 ± 0.9	
	11	227.7, 31.7, 82.3	14° from (101)	79.7 ± 1.0	
	3	57.5, 43.5, 71.3	15° from (101)	78.3 ± 0.8	
	6	326.1, 43.1, 69.3	15° from (101)	79.0 ± 0.5	
	9	60.8, 36.5, 65.3	19° from (101)	78.6 ± 0.7	
Near [001]	7	188.9, 8.7, 32.9	13° from (001)	80.6 ± 0.1	80.5
	14	231.5, 19.4, 52.5	19° from (001)	81.3 ± 1.0	
	4	274.2, 25.0, 73.7	28° from (001)	79.5 ± 0.2	